Journal of Dynamic Behavior of Materials (2018) 4:34–55
https://doi.org/10.1007/s40870-017-0135-1

On the Processing of Spalling Experiments. Part I: Identification of the Dynamic Tensile Strength of Concrete

P. Forquin[1] · **B. Lukić**[1]

Received: 12 June 2017 / Accepted: 11 October 2017 / Published online: 21 November 2017

Abstract

The spalling technique based on the use of a single Hopkinson bar put in contact with the tested sample has been widely adopted as a reliable method for obtaining the tensile response of concrete and rock-like materials at strain rates up-to 200 s^{-1}. However, the traditional processing method, based on the use of Novikov acoustic approach and the rear face velocity measurement, remains quite questionable due to strong approximations of this data processing method. Recently a new technique for deriving cross-sectional stress fields of a spalling sample filmed with an ultra-high speed camera and based on using the full field measurements and the virtual fields method (VFM) was proposed. In the present work, this topic is perused by performing several spalling tests on ordinary concrete at high acquisition speed of 1Mfps to accurately measure the tensile strength, Young's modulus, strain-rate at failure and stress–strain response of concrete at high strain-rate. The stress–strain curves contain more measurement points for a more reliable identification. The observed tensile stiffness is up-to 50% lower than the initial compressive stiffness and the obtained peak stress was about 20% lower than the one obtained by applying the Novikov method. In order to support this claim, numerical simulations were performed to show that the change of stiffness between compression and tension highly affects the rear-face velocity profile. This further suggests that the processing based only on the velocity "pullback" is quite sensitive and can produce an overestimate of the tensile strength in concrete and rock-like materials.

Keywords Tensile strength · Spalling · Concrete · Novikov formula · Ultra-high speed photography · Virtual fields method

Introduction

Concrete is one of the most used building materials, thanks to its low density, high compressive strength but also availability of its constituents and straightforward manufacturing. Nevertheless, its range of application in civil engineering has been restricted by its low tensile strength and quasi-brittle response. For this reason, in most engineering codes concrete is usually considered to have only compressive bearing capacity in quasi-static loading conditions while the tensile stresses are transferred to the internal steel reinforcement. However, in concrete structures exposed to sever transient dynamic solicitations (e.g. projectile impacts, blasts or explosions), the ultimate material response can be highly affected by the complex stress states and high deformation rates that evolve in the material [1, 2]. Under such extreme conditions, the reflection of compressive waves causes tensile waves to be generated which lead to intense tensile damage known as spalling [3]. Since several decades, studies have indicated pronounced strain rate sensitivity of concrete in dynamic tension, namely the increase of tensile strength with the increase of the loading rate [4, 5]. This suggests that, if well understood, the concrete dynamic tensile strength could be exploited during the structural design, leading to better engineering solutions and substantial economical savings.

However, despite the large amount of research conducted, obtaining reliable test results still represents a great challenge. The difficulties are mainly associated to the ways of experimentally measuring the low tensile strength and small failure strain inside the specimen, which are an inherit

---

Electronic supplementary material The online version of this article doi:10.1007/s40870-017-0135-1) contains supplementary material, which is available to authorized users.

✉ P. Forquin
pascal.forquin@3sr-grenoble.fr

[1] Institute of Engineering, CNRS, Grenoble INP, University of Grenoble, Alpes 3SR, 38000 Grenoble, France

characteristic for this material. To this end, numerous experimental techniques have been devised in order to investigate concrete's dynamic tensile response. A large number is based on the well-established split Hopkinson pressure bar (SHPB) system. Some of these experimental methods rely on applying a direct tension through gravity driven loading [6–11] or by using a pre-stressed cable and the so called Hopkinson bar bundle [12–14]. Other techniques also include split tension (better known as the Brazilian test) [15, 16], semi-circular bending [17, 18] and three-point bending tests [19–21] where the geometry of the sample is such that it favours tensile failure. However, all of the above mentioned techniques rely on assumptions how the experimental data are analysed. Particularly, the fact that the specimen stays in the mechanical equilibrium throughout the test represents a strong limitation which does not allow obtaining data in regimes where inertial effects are significant. Thus, these methods are limited to lower rates of deformation, up-to about 10 s^{-1} which represents a lower limit of the tensile strength enhancement [22, 23].

For reaching higher strain rates, up-to a few hundred s^{-1}, the so-called spalling technique which uses only the input bar of the SHPB system has been widely adopted [24–29]. The method relies on the reflection of the compressive wave into a tensile load from the sample's free surface, which is in contact with the input bar [30]. The traditional processing of the spalling experiments relies on the use of strain gauge and velocity measurements [25, 30]: the peak stress is obtained by measuring the velocity pull-back at the sample's free surface and by using the so-called Novikov formula [31]. This processing is currently considered to provide the most accurate result and is being widely adopted for obtaining tensile strength of concrete-like materials [25, 27, 30, 32, 33]. Nevertheless, this method still relies on some strong assumptions that question the validity of the obtained spall data. Firstly, it uses a linear acoustic approximation to obtain the ultimate spall strength. Next, it assumes a linear elastic material behaviour until the peak tensile strength is reached. Finally, it relies on the assumption that the velocity rebound results from one instantaneous spall fracture initiated in the sample. In this work, it will be concluded that these assumptions can lead to overestimation of the spall strength when heterogeneous materials, such as concrete, are in question. Commonly made as a mixture of cement, sand and aggregates, concrete exhibits a complex internal microstructure. Consequently it displays a non-linear behaviour before the failure is reached. Furthermore, spallation is generally a process that involves nucleation, growth and coalescence of newly generated cracks which may not happen instantaneously but rather takes place over several microseconds. Moreover, the evidence of diffuse damage preceding the ultimate tensile failure has been well documented in both experimental observations [30, 32] and numerical simulation works [34–38] which can imply that the Novikov formula is no longer valid since the measured pullback velocity contains information about the entire damage history that occured in the sample.

Previously mentioned experimental method depends only on the instantaneous point-wise measurements (strain gauges, laser interferometer) for obtaining the peak stress and the corresponding strain rate, which provide limited information of the change of stress in the sample as well as the post peak response. An innovative approach to processing the spalling experiments has been proposed by Pierron and Forquin [39] that uses full field measurements. It is based on the virtual fields method and the use of an ultra-high speed camera to film a grid bonded onto the sample surface in order to measure the stress level and apparent Young's modulus in a concrete sample during the test. The authors observed a substantial decrease in average stiffness in the tensile stage of the test. Moreover, in all tested samples, the peak tensile stress observed was up-to 30% lower than the one obtained with the Novikov processing. On the other hand, it was not clearly established which technique provides more reliable result.

This question is perused in the present work. By testing several concrete samples with the camera interframe time set to 1 μs and comparing the results obtained from classical processing with results from full-field measurements, it is shown that the non-linear behaviour begins before the principle macro-fracture. This indicates that the assumption of the linear elasticity up-to the peak is no longer valid. The obtained results also showed that the dynamic Young's modulus in tension highly differs from the values obtained in the compressive stage. Since the method proposed in [39] only relies on the displacement measurements, the accuracy of the identified material stiffness heavily depends on the full-field measurement parameters such as camera performance and noise, spatial and temporal resolution. Therefore, further tools are necessary to verify the validity of the obtained results from full field measurements. This is presently addressed by simulating the spalling experiments with damage model known as the *Mazars model* [40] which has already been proved to well reproduce the rear face velocity of a spalling test [41]. Finally, it was shown that by changing the Young's modulus in dynamic tension without changing the tensile failure strength, the rear face velocity exhibits a change in rebound that can lead to misinterpretation of the spall strength obtained with the Novikov processing; suggesting that the presented processing method provides a more reliable spall results.

Experimental Procedure

Spalling Test and Materials

The spalling technique was first introduced by Klepaczko and Brara [24], where a cylindrical sample was placed in contact with the metallic input bar at one end, while on the other end a generated incident compressive pulse travels through the bar, transmits to the sample and reflects from the sample's free-end as a tensile wave that ultimately leads to spall fracturing. Since then it has been adopted as a reliable way of determining the intrinsic dynamic tensile strength of brittle materials [22, 42]. Besides its simplicity, the main advantage of this experimental technique is that it relies on the sample's intentional unbalanced state. The incident compressive pulse can be induced as shock wave by a pyrotechnical charge [26, 43] or by a projectile impacting the input bar [24, 25]. The input bar is usually equipped with one or several strain gauges aimed at capturing the motion of the incident wave through the bar.

Several methods can be found in the literature for deducing the peak tensile strength from the spalling tests. One of the methods relies on the reconstruction of the fictive elastic axial stress from the analytical superposition of uniaxial elastic waves assuming that the peak stress occurs at the location of the observed macro-fracture as for example in [24, 44, 45], another method is to capture the residual velocity of spall fragments obtained from images of a high-speed camera [24] and finally the method of using the measurement of sample's rear face velocity and the so-called velocity rebound [25, 38]. These processing techniques for deriving the spall strength were detailed and analysed in [30], where it was shown that the first two methods mentioned can lead to strong overestimation of the deduced peak stress. On the other hand, it was noted that the processing method based on the measurement of the pull-back velocity on the sample's free end and the Novikov acoustic approximation [31] can be considered to provide more accurate results regarding the concrete's apparent tensile strength. The measurement of the sample's rear face velocity can be obtained by using a miniature accelerometer, or by using a laser interferometer. The latter presents a clear advantage over the accelerometer which can introduce local inertial effects that disrupt the measured velocity profile and possibly fail the sample locally [30].

In the present work, full field displacement data obtained by filming the sample surface with an ultra-high speed camera are exploited in order to derive the values of dynamic Young's modulus and average stress in sample cross-section. Dynamic tensile experiments based on the spalling technique have been performed on three samples of ordinary concrete known as R30A7 [38, 46, 47] utilising both traditional measurements and full field measurements as shown in Fig. 1. Concrete, as many other geomaterials, has a pronounced microstructure that consists of voids and a pre-existing cracks network, which influences its mechanical response to applied loading [48, 49]. The concrete used in this study is composed of hard siliceous aggregates with maximum grain size of 8 mm. The samples of 45 mm diameter and 140 mm in length were cored out from large blocks and then rectified to obtain a flattened outer surface of 23 mm with used for gluing the grid pattern.

It is necessary to mention that the concrete samples had to undergo a drying procedure before testing due to transferring method used to deposit the grid onto sample surface. Indeed, the fact that the sample surface has to be instrumented by depositing a perfect regular pattern represents a drawback of this method from a practical point of view. In general, there are several techniques for applying the grid pattern onto the sample and the choice mainly depends on their frequency [50]. The most reliable technique for grids of 1 mm pitch and lower, which allows a good adhesion between the surface

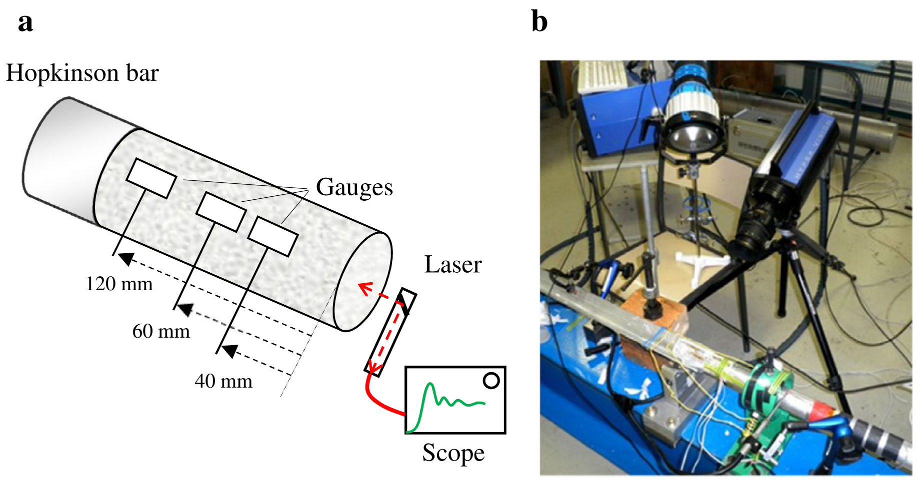

Fig. 1 **a** Point-wise instrumentation of the spalling test; **b** spalling set-up with full field measurements

and the photosensitive film has been proposed by the authors in [51]. First the flat surface is cut and well-polished so it is smooth and parallel with the axis of the sample. Next, bi-component epoxy glue (Epotechny E504), which is of white colour when fully cured, is used to assure a well contrasted grid. The photographic film and the sample surface are then coated with a thin layer of white epoxy glue, merged and left under a constant pressure of about 5 kPa. The pressure allows excessive glue to go out and to flatten the substrate to the sample surface. The curing process is considered as the limitation of the deposition method as the sample has to be left to cure at temperature of 40° for at least 40 h. In the present case, the samples have been left for several days in order to ensure the best possible adhesion and a good transfer of the grid on the surface. After curing, the film has been slowly peeled off the sample surface which results in black lines being transferred onto the specimen surface.

The assumption of a good kinematic transfer between the substrate and the grid along with the assumption that the grid does not change the global material response, are the prerequisites of this full field measurement method. These assumptions have been adopted here as the resulting thickness of the glue (being around 0.2 mm) can be regarded as negligible compared to samples' cross-section and as small strains were measured.

Virtual Fields Method

The Virtual Fields Method (VFM) [52] can be used to extract the material constitutive parameters from full field measurements. Relying on the principle of virtual work and taking advantage of the sample non-equilibrium state throughout the spalling experiment, the derived acceleration fields can be used as an alternative 'load cell' without any need of other external force measurement. The idea of exploiting the inertial forces as a measurement tool can be used in a wide range of material identification procedures. It was firstly proposed and successfully applied for identification of damping properties of thin vibrating plates [53, 54]. Later, the concept was extended to identification of material stiffness parameters in intermediate [55] and high strain rate testing of composite materials [56] as well as rubber materials [57, 58]. Finally, a recent study conducted on ultrasonic excitation of surrogate bone material allowed identifying entire maps of Young's modulus showing that the method can be extended to the wide range of original applications [59, 60].

During a spalling test the stress in the sample is generally considered to be uniaxial. Using this characteristic and the principle of virtual work, it is possible to reconstruct the average longitudinal stress in any cross-section and any instant visualized with the UHS camera (at a given longitudinal position of x coordinate, $x = 0$ corresponding to the free end of the sample) by introducing a rigid body like virtual field. The stress is defined by averaging the longitudinal acceleration fields over the area between the considered cross-section at the position x and the free-end as following:

$$\overline{\sigma_x(x,t)} = -\rho\, b(x)\, \overline{a_x(x,t)} \tag{1}$$

where t corresponds to the current time, $\overline{\sigma_x(x,t)}$ denotes the mean axial stress in the observed cross section at location x, ρ is the density of the material, $b(x)$ corresponds to the length between the observed cross-section and the free-end, and $\overline{a_x(x,t)}$ corresponds to the mean acceleration between the cross-section and the free-end.

The derived acceleration fields can also be used to obtain the description of the average material Young's modulus at each instant of the test in compression [55]. By introducing special virtual field in the dynamic equilibrium equation as a differentiable function $f(x)$ of the longitudinal coordinate x such that cancels out the contribution of the traction component at the opposite boundary of the field of view to the free end, the average Young's modulus at each time step of the test can be defined through the acceleration virtual work and internal virtual work as:

$$E_{dyn}(t) = \rho \left(\frac{\overline{a_x(t) f(x)}}{\overline{\varepsilon_x(t) f'(x)}} \right) \tag{2}$$

where the fields of virtual work $\overline{a_x(t) f(x)}$ and $\overline{\varepsilon_x(t) f'(x)}$ are averaged from the cross-section to the free-end. In general there exists infinite number of virtual fields that could satisfy these conditions; however the best is to choose those that maximize both fractions of the Eq. (2). In the present case, the chosen virtual fields are obtained directly from the measured full field displacements. This is done by first averaging the measured axial displacement field in y direction at each imaged frame. Then, to each obtained displacement vector that only depends on x a polynomial fitting in the least squares sense is performed. In this work, the 8th degree polynomial is used and the 2D virtual fields maps are obtained by expending back the obtained polynomial expressions in order to obtain fields that only depend on the direction of axial displacement as required in Eq. (2). Finally, a constant value is added to each virtual field in order to satisfy the condition $[f(x = l) = 0]$.

What is worth pointing out is that the two presented equations are independent regardless the material constitutive behaviour as they are obtained from the principle of virtual work which is a simple reformulation of Newton's second law and conservation of momentum. The required acceleration fields can be retrieved as the second derivative of displacement fields, where the displacements are obtained with one of the non-contact optical measurement techniques.

Full Field Measurements and Ultra High Speed Photography

Although digital image correlation (DIC) is currently one of the most popular full-field measurement technique, another alternative is the grid method [61]. The grid method is suitable for obtaining small in-plain displacement field measurements [62], and is still commonly used when high strain rate dynamic testing is in question [56, 63]. This is mainly due to its easy implementation as well as high measurement resolution as discussed in [64]. This technique, for now, provides a better compromise between spatial resolution and measurement resolution, which is an important factor when ultra-high speed imaging is used owing to limited pixel count of currently available acquisition systems. On the other hand possible benefits of using digital image correlation as a tool for obtaining full-field displacement measurements during a spalling test have been suggested in [65].

The grid method is a full-field image analysis method for non-contact deformation measurements of the sample surface, which is based on determining the phase change between the reference and the deformed image on the spatial carrier deposited on the framed surface. Detailed presentation of the grid method is out of the scope of this paper. However, the interested reader is encouraged to refer to recent extensive review of this technique published in [66]. During the spalling experiments a Shimadzu HPV-1 camera, able to reach 1 µs interframe time with 102 acquired frames, was used to film the grid of 1 mm pitch glued on the sample surface. This camera relies on the so called in-situ storing technology where an integrated memory is dedicated to each pixel on the imagining sensor [67, 68]. An overview of the evolution of in-situ acquisition systems and some future expectations are provided in [69]. However, these imaging systems still suffer from some limitations that can impair their metrological performance, such as a limited number of image pixels. The image size obtained by the camera used in the present study is of 312 × 260 pixels, which directly influences the choice of grid pixel sampling size and forces a trade-off between the size of the framed surface and the information measurement precision. On one hand, increasing the number of pixels per period used for grid sampling can reduce the standard deviation of the measured quantity as discussed in [70], on the other hand, the size of the observation zone decreases and the macro-crack formation can occur outside of the recorded zone. Therefore, the information of damage processes that lead to failure can be completely lost. For these reasons, the five pixels per period of the grid image were used and the observation window in that case was 62 × 24 mm where a measurement point is obtained at each millimetre distance. The image intensity pattern directly encodes the measured physical quantity through its intensity variation. Therefore, a non-constant spatial lightning throughout the grid image can introduce errors that generally evolve through the obtained strain maps [66]. Even though camera's 8bit dynamic range is able to capture 256 grey levels, in order to avoid these effects the lightning source has been adjusted so that the grid was exposed to an almost uniform spatial illumination field. This can be seen on Fig. 2a where one reference grid image is shown.

For the reasons already suggested in [39], the lightning conditions were kept in lower range of grey levels in order to skirt around the saturation effects characteristic for this specific acquisition system as detailed in [71]. In the cited work the authors also observed a specific temporal noise that manifests as an underexposure of each 12th recorded frame. This can be seen in the Fig. 2b where the average grey level variation of the framed grid is given for the entire sequence of 102 frames with the interframe time of 1 µs. It can be observed that during first 12 frames there is large fluctuation of the grey level intensity until the sensor stabilizes, similar is observed in the last 12 frames. However, the frames

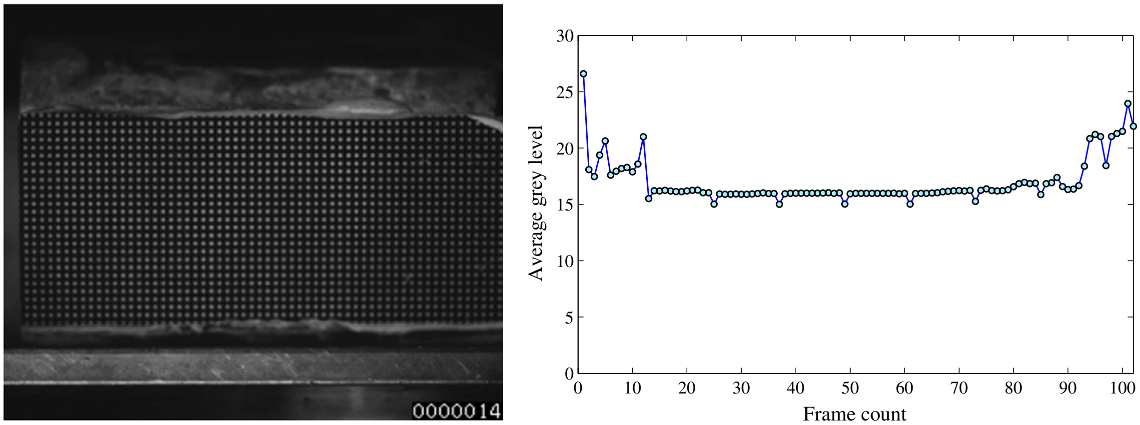

Fig. 2 **a** Reference grid image (Tiff015); **b** average grey level intensity profile of the acquisition R30A7-1

starting from 13 to 90 seem quite stable except of the temporal fluctuation that manifests each 12 frames. This problem was tackled here by deleting the over-exposed frames and replacing them with the mean of the two adjacent ones as advised in [71]. Nevertheless, the image processing time still remains reasonably short and the entire identification takes just below one hour, which can be also considered as one of the advantages of the adopted method. Aside all the difficulties presented, it will be shown that even in this limited conditions it is possible to extract abundance of meaningful data from the acquired images that allow much better understanding of the material actual dynamic response. Furthermore, the future development of the UHS acquisition systems will bring only benefit to the currently applied testing methodology, keeping an accent on the stability of image forming.

Experimental Results

Measurement Results

In this section, results of three spalling tests that have been performed on common concrete samples using the experimental measurement set-up shown in Fig. 1 will be presented. The data retrieved from one spalling test consist of both standard point-wise measurements, such as strain gauges and laser interferometer, and in-plane full field displacement maps obtained from grid images captured with the means of ultra-high speed photography. The measured data from both techniques are compared and it was noted that the traditional processing leads to large overestimation of concrete's dynamic tensile strength.

Standard Measurements

The traditional processing of the spalling test is based on the method that has been previously proposed and validated by Erzar and Forquin [30]. The laser interferometer pointed towards the sample free-end provides the measurement of the particle velocity profile throughout the entire test. Knowing the material density and the material wave speed (Table 1), the apparent failure strength can be deduced by observing the so called velocity 'pull-back' and employing the Novikov formula [31] as:

$$\sigma_{laser} = 1/2\, \rho\, C_0 V_{pb} \tag{3}$$

The pull-back velocity (V_{pb}) represents the difference between the peak particle speed (corresponding to the point of compression to tension transition) and the velocity at the first rebound. This processing relies on the assumption of unidimensional linear elastic wave propagation until the peak failure stress inside the sample is reached. Three strain gauges glued on the sample surface are located at different distances from the samples free-end as to capture the wave propagation and reflection until the tensile macro failure occurs. The strain gauge close to the contact surface serves to capture the compressive pulse transmitted from the Hopkinson bar to the sample and to acquire the material wave speed. This is obtained by performing a temporal shift of the data captured by the compressive strain gauge strain gauge to match the velocity profile. One such set of data is presented in Fig. 3 for one tested concrete sample (Tomo1), where the gauge and laser data are converted into values of axial stress assuming unidirectional elastic wave propagation.

When referring to the Fig. 3 it can be observed that the time shifted axial stress curves obtained from the strain gauge measurement ($\sigma = E\, \varepsilon_{gauge}$) and from the rear face velocity ($\sigma = 1/2\, \rho\, C_0\, V_{laser}$) overlap quite well up-to the point when the peak stress is reached, after which the two curves are characterised with a different descending slope. The peak corresponds to the point where the transition from compressive to tensile loading stage starts and when the wave reflection starts taking place. The observed difference after the peak can be an indication of a different material response in compression and tension, namely due

Table 1 Experimental specification of three spalling tests conducted on R30A7 concrete

Sample	Material	Density (kg/m^3)	Impact speed (m/s)	Wave speed (m/s)
R30A7-3	R30A7	2374	11	4250
R30A7-1	R30A7	2269	8.18	3810
R30A7-2	R30A7	2359	11.24	4250

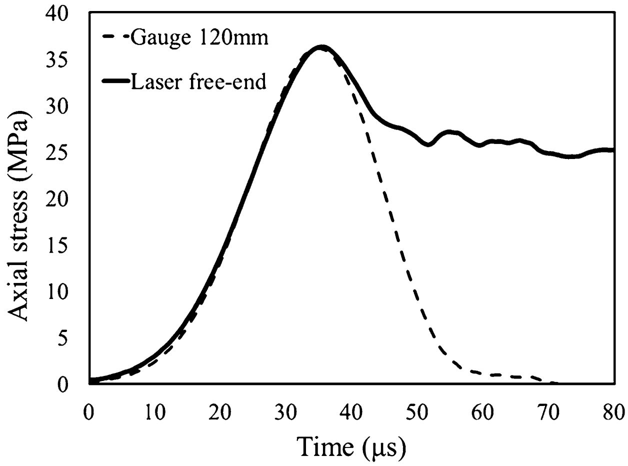

Fig. 3 Method for obtaining the material wave speed: shifted compressive pulse to the pulse registered on the free-end (R30A7-1)

to a possible difference in stiffness. This will be addressed in the following part by processing the full field experimental measurements and later on discussed in Sect. "Validation with numerical simulation" using FE numerical simulations.

Full Field Deformation Measurements

As previously mentioned, the temporally resolved in-plane displacements fields are obtained by processing the grey level grid images of sample surface framed with an ultra-high speed camera. Sequences of 102 images are obtained for each test with the camera acquisition speed set to 1 Mfps with the exposure time of 1 µs. The obtained images were processed using the information presented in Table 2. The displacement maps for one tested specimen, R30A7-1 are given at the several frames preceding the fracture in Fig. 4. The displacement map at 70 µs from the beginning of the recording process clearly shows presence of several displacement-discontinuities, namely at around 30 and 40 mm from free surface. The entire evolution of the measured displacement maps with the evolution of average axial surface displacement are provided in the 'Supplementary material: Video 1'. From the video it can be seen that the crack appearing at 30 mm does not appear to fully open by the end of the test but rather stays closed, likely due to stress relaxation induced by the growth of the macro-crack appearing at 40 mm that ultimately fails the sample.

From the obtained displacement fields the strain maps can be derived. The strain fields are derived with the same procedure as used in [39]. A local fit of the weighted second-degree polynomial is performed on a span radius of 10 displacement points using a diffuse approximation approach [72, 73]. A larger window for strain derivation is used in order to reduce the effects of spatial noise coming from the acquisition system. In complementary to previously shown displacement maps, the Fig. 5 displays the global axial strain obtained as an average strain evolution on the entire surface visualized with the camera. It can be observed that the global strain does not exhibit a pronounced change at times of the formation of the macro-crack, namely 70 µs. The entire evolution of the measured strain maps with the evolution of average axial strain are provided in the 'Supplementary material: Video 2'.

Identification of Material Response

In the following the virtual fields method is used to identify the material response of the three tested samples by extracting meaningful results of stress evolution inside the sample as well as global and local material stiffness from the acceleration data. Then, the stress–strain response can be

Table 2 Imaging measurement performance and processing information

Camera	Shimadzu HPV-1
Pixel array size	312 × 260 pixels
Frame rate	1 Mfps
Exposure time	1 µs (1/frame rate)
Field of view	23 × 60 mm
Number of frame	102
Grid method	
Pitch	1 mm
Sampling	5 Pixels per period (N)
Reference image	15
Displacement	
Window	Triangular
Spatial resolution	9 Pixels (2N – 1)
Temporal resolution	1 µs
Strain	
Smoothing method	Diffuse approximation, 10 pixel radius
Spatial resolution	10 mm
Temporal resolution	1 µs
Strain rate	
Smoothing method	Second-order polynomial fit over 5 temporal strain points
Temporal resolution	5 µs
Acceleration	
Smoothing method	Second-order polynomial fit over 11 temporal strain points
Temporal resolution	11 µs

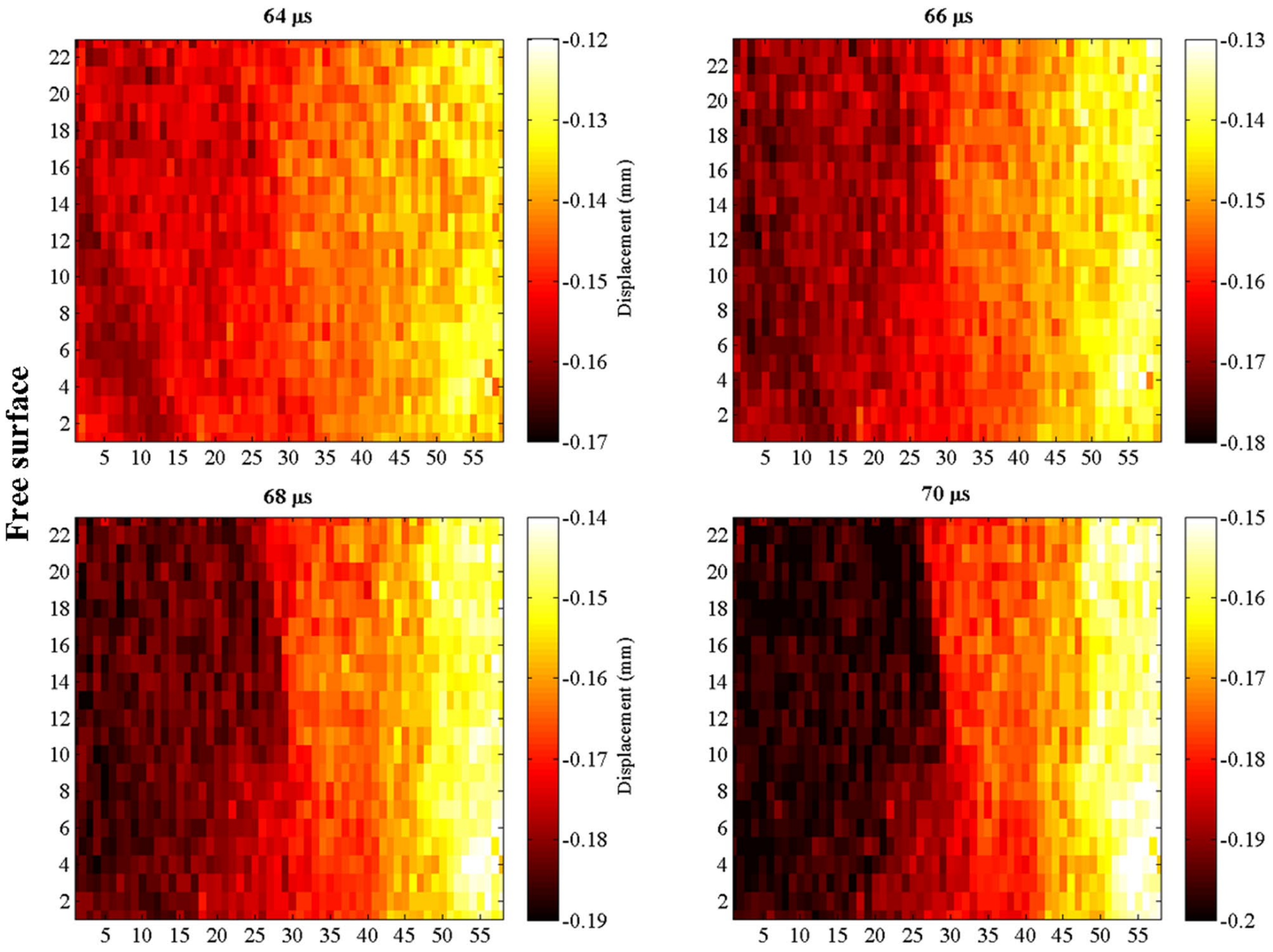

Fig. 4 Full field displacement maps of the concrete sample surface at different times preceding the macro-fracture clearly show two discontinuities that manifest as displacement jumps at location of 30 and 40 mm (spatial size of presented maps presents horizontal and vertical distribution of measurement points in millimetres). Sample R30A7-1

identified from these results without the need of any other external measurement and most importantly, no assumption on the material behaviour. It was observed that the stiffness of the tested concrete samples largely differed depending on the stage of the loading (compression to tension). Furthermore, the estimated peak strength from the stress–strain curves was in all cases lower than the one obtained with traditional processing. Finally, the problematic associated to determining the strain rate at peak stress which is desired information to be obtained from these tests is addressed.

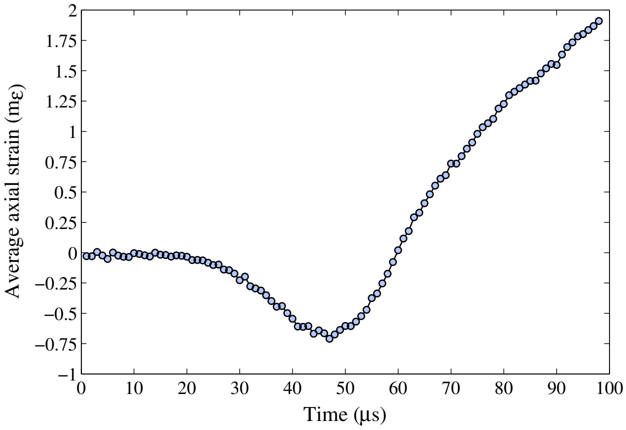

Fig. 5 Global axial strain obtained as averaged strain on the entire observation surface of the R30A7-1 specimen

Stress and Strain Analysis

It was previously shown in Sect. "Full field measurements and Ultra High Speed photography" that by introducing a rigid body virtual field in the equation of principle of virtual work and by assuming perfect uniaxial loading conditions, the acting inertia can be utilised as a direct force measurement throughout the spalling test. Then, the average stress in every observed cross section can be calculated as a function of the axial acceleration averaged from sample free-end to the observed location. The great benefit of this method is that the entire fields of information are embedded in the images captured with the ultra-high speed camera, which represent the only necessary measurement to process the entire test. After obtaining the in-plane displacement maps of the sample surface, it is necessary to perform the second degree temporal derivation of the displacement fields in order to obtain the acceleration maps. This is presently performed with applying the temporal filtering of the raw displacement measurements [74]. A second order polynomial fit is performed over a temporal sliding window of 11 images to decrease signal-to-noise ratio and evaluate the derivate in the central point of the moving subset. This type of temporal data processing was adopted from this point onward for all the tested samples.

The right column of the Fig. 6 shows the axial stress profiles reconstructed for all longitudinal positions for each tested concrete sample. Two distinct zones that correspond to the propagation of the compressive and reflected tensile wave can be observed. The compressive stage lasts about 40 µs while the tensile stage is governed by the concrete's tensile strength and seems to last about 15 µs after which the stress values are close to zero. It can be also observed that the stress is much larger during the first stage of the compressive loading than during the second tensile loading stage. Finally, a strongly homogeneous stress field can be observed during the tensile loading stage. When referring back to the space–time maps of strains, on the left hand side of Fig. 6, it is clear that the low stress values in tension are caused by samples' failure that manifests through the presence of several strain localisations. Interestingly, strain localisation can already be observed at 30 mm from the free surface even though after the tests only cracks at 40 mm were visible to the eye in the samples R30A7-3 and R30A7-1. This is due to the fact that the crack at 30 mm is in fact closed micro-crack as already mentioned when displacements maps were analysed. This can be better seen in the 3D strain maps given in the 'Supporting material: *3D graphs*' of this article where the strain concentration at 30 mm from free end are lower than the values at the location of the observed macro-crack.

From the illustrated stress and strain maps, the local stress–strain curves can be obtained in each cross-section of the tested samples. Those of the highest interest are the locations that correspond to the positions of crack formation where the non-linear material response is expected. The tested samples were also instrumented with strain gauges that are glued at a certain distance from the sample's free-end as shown in Fig. 1. The strain gauge generally introduces minor spatial filtering of the deformation data due to their physical size. Therefore, a virtual gauge can be chosen to process the stress and strain fields as to provide additional spatial smoothing of the data. The area chosen was of 20×1 mm which represents characteristic grid size of conventional polyester foil gauges used in this type of experiment. Figure 7 represents the reconstructed stress–strain response of three concrete samples applying a virtual gauge at 30 mm and 40 mm from free-end. In each figure the starting point is marked after which the stress values start to increase.

Since the spalling test provides a unidirectional stress state, the slope of the curves describes Young's modulus of the sample at these locations. It can be observed that the response in all cases is reasonably linear in compression. However, the response of the material is different during the compressive and tensile loading stage, for that reason two linear regressions are performed. The first regression line is performed on the set of stress–strain points that construct the compressive stage, neglecting the first several points that correspond to low acceleration levels. The second regression is performed on the tensile part of the curve up-to the point which corresponds to the peak stress. It becomes clear that the slopes of the regression lines differ from compressive to tensile stage pointing towards different material responses. Furthermore, there is an indication of non-linear behaviour few moments prior the peak stress. The curves show that the stress values flat out after reaching a peak that could be associated with the progressive damage process prior the failure. The obtained values of Young's modulus and the maximal tensile stresses from the presented stress-strain curves are summarised in Table 3.

Interestingly, for all tested samples the maximal stress reached seems to be lower than the values obtained with traditional Novikov processing, presented in Table 3. As discussed in the previous work of the main author, the reason for this is that the standard Novikov processing technique for obtaining the ultimate stress, relies on the assumption of the propagation of linear-elastic waves up to the failure. Whereas, it is clear from the reconstructed stress–strain curves that the response exhibits certain non-linear behaviour far from the macro-crack plane, owing to the progressive growth of cracks. Finally, the results clearly show that the Young's modulus in the dynamic tension is 40–70% lower than the Young's modulus identified during the compressive response. This reduction of tensile stiffness could be explained to some extent by the possible presence of initial defaults as it has been observed in previous works on dynamic tensile testing of granite rock material [75].

Strain Rate

Another difficult challenge associated to the characterisation of dynamic tensile response of concrete is to well define both the peak stress and corresponding strain rate

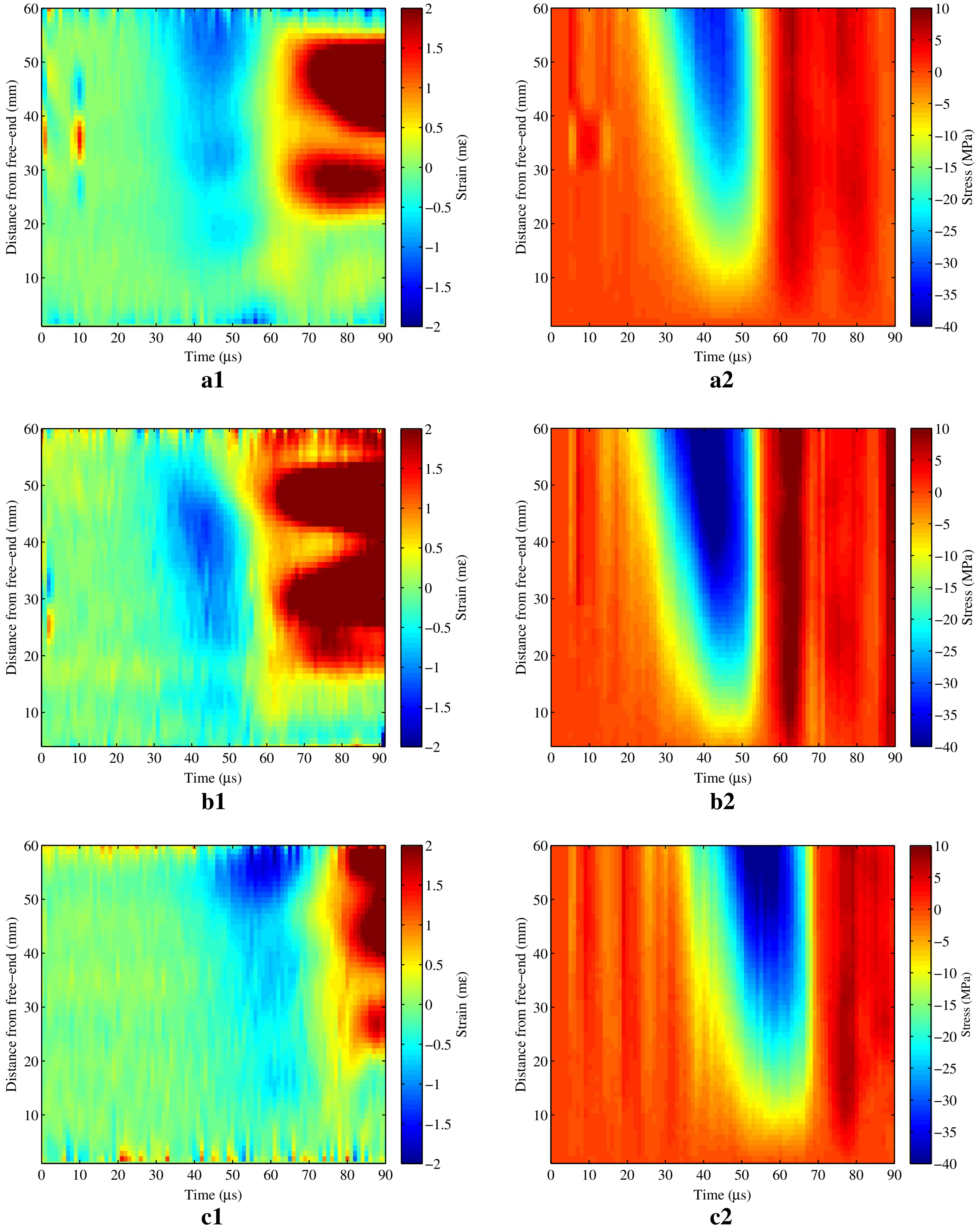

Fig. 6 Space–time maps of stress and strain for three tested concrete samples: **a1**:**a2**–sample R30A7-1; **b1**:**b2**-sample R30A7-2; **c1**:**c2**–sample R30A7-3

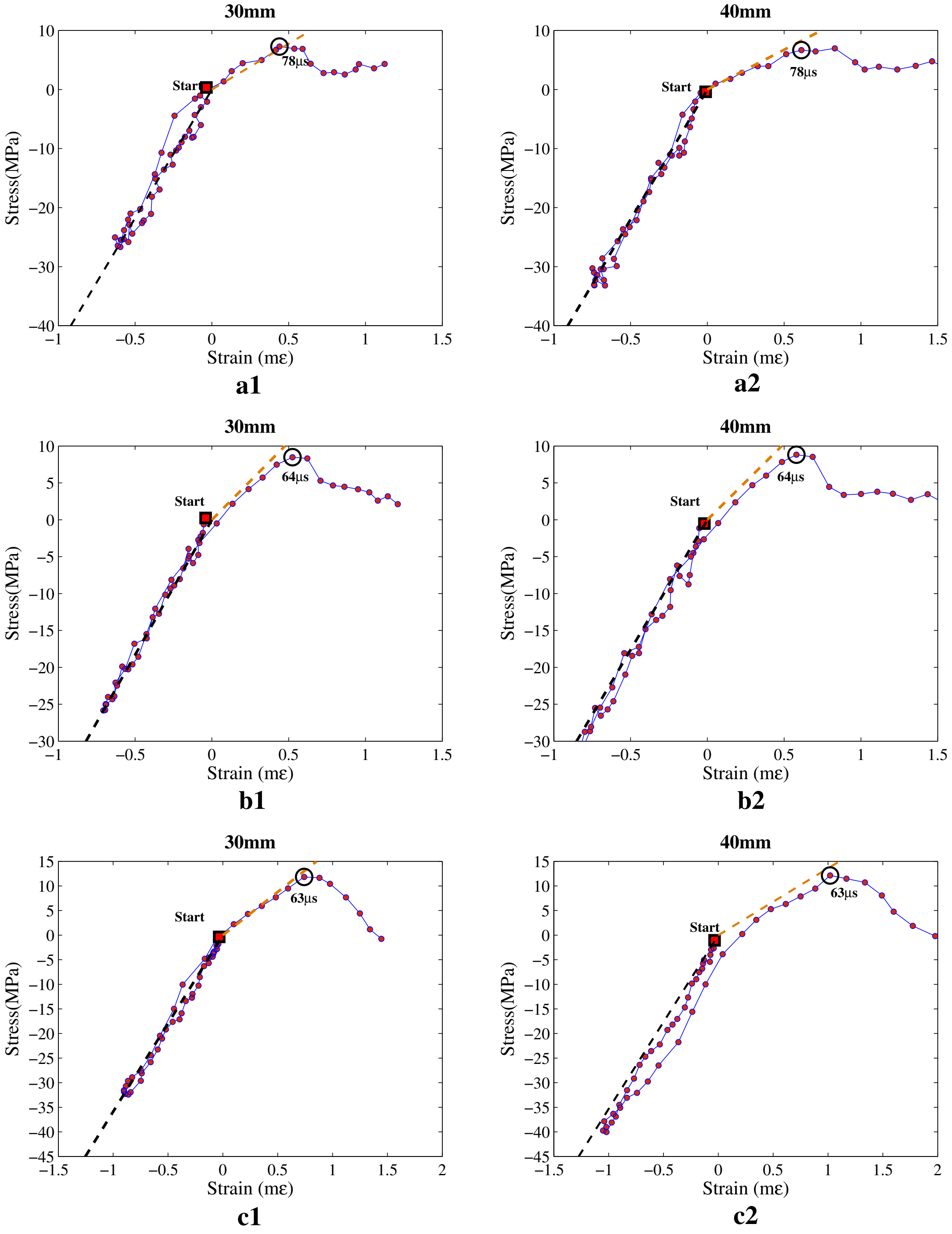

Fig. 7 Reconstructed stress–strain curves of a virtual gauge for three tested concrete samples at 30 and 40 mm from free end: **a1**:**a2**–sample R30A7-3; **b1**:**b2**-sample R30A7-1; **c1**:**c2**–sample R30A7-2

in the tested specimens. In fact, both stress and strain rate can considerably vary throughout the spall test. Obtaining accurate values of strain rate at failure is a prerequisite for well understanding the strength increase with the rise in rates of deformation. One way of controlling the strain rate is to devise experimental techniques that maintain mainly constant evolution of strain rate close to the failure location. In the present work, a pulse shaping technique of so-called

Table 3 Results of identification from the reconstructed stress–strain curves

Sample	Gauge position (mm)	Young's modulus compression E_c (GPa)	Strain rate (s^{-1})	Young's modulus Tension E_t (GPa)	Dissymmetry factor E_t/E_c (%)	Tensile stress (MPa)	Time to peak (µs)	Novikov (MPa)
R30A7-3	30	43.54		16.72	38.54	7.27	7	/
	40	44.06	60–100	13.47	30.65	6.96	7	
R30A7-1	30	36.61		21.03	57.45	8.48	6	10.6
	40	35.22	80–100	20.65	58.56	8.81	6	
R30A7-2	30	35.89		17.65	49.11	11.84	6	15.1
	40	35.33	120–130	15.25	43.21	12.14	7	

spherical cap projectile is used that was numerically optimised and verified in [30, 76]. This technique decreases the variation of strain rate and reduces the initial shock effects by increasing the rising time of the loading pulse. The identification of the strain rate at failure, as presented in [30], starts off by obtaining the apparent failure strength of the material from the rear face velocity profile. Next, the fictive stress curves obtained from the strain gauge history (i.e. $E_{dyn}.\varepsilon_{gauge}$) are traced up-to the deduced failure stress to obtain the time at failure. It has to be mentioned that the Young's modulus used is the one identified by wave speed analysis (i.e. compressive stiffness). Then by simple derivation of the strain data obtained from the gauges glued on the sample surface an interval of strain rate at failure can be obtained. Change of axial stress as a function of strain rate can be reconstructed directly from the full field data.

In that case, only one temporal derivation of strain is necessary which is presently performed by deriving a second order polynomial fit over a sliding window of 5 strain points. The 20 point virtual gauge is introduced to provide additional smoothing to the reconstructed curves that are shown in Fig. 8 for locations at 30, 40 and 50 mm from the free end. In the useful part of the plot (positive stress and strain rate) low variations of strain rate close to the point of the macro fracture can be concluded from curves at 30 and 40 mm. The variation of strain rate increases at the location 50 mm when the failure takes place and the axial stress drastically decreases.

Another way of obtaining the values of strain rate at peak stress is to analyze the strain rate history at the positions of 30 and 40 mm from the free end as shown in Fig. 9. The vertical lines mark the time when the stress in the samples reaches the peak, which is obtained from the reconstructed stress–strain curves shown in Fig. 7. Additionally, measurement data obtained from actual gauges glued at 40 mm from the sample free-end are shown for comparison. It can be seen that the results obtained from the virtual gauge and from real gauge at the same distance coincides well and the small differences can be attributed to the local heterogeneities of the concrete material.

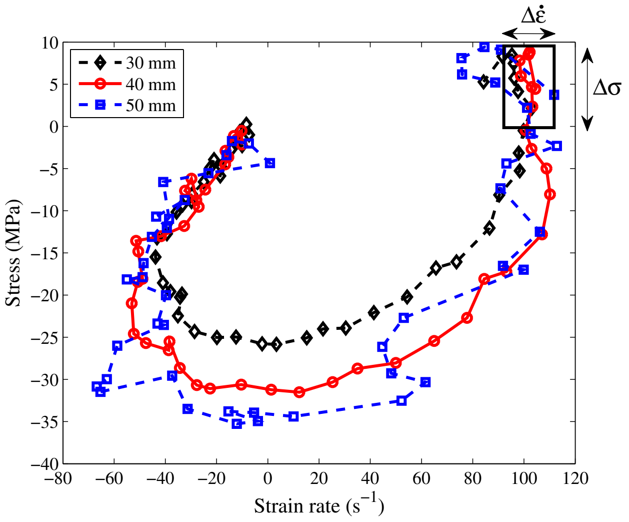

Fig. 8 Strain-rate as a function of the stress level obtained from full field measurements for the R30A7-1 test

Next the strain rate at stress peak can be estimated. Here, several techniques will be compared just for sake of showing that even up to today the measurement of strain rate remains quite difficult to obtain. First technique relies on processing only the point-wise measurements as proposed in [30] (Method 1), the second one utilizes the same method but with the strength obtained from the stress–strain curves reconstructed from full field measurements (Method 2). In the third method, the failure stress and strain rates are provided for two locations along the sample axis by only using the virtual gauge measurement from the data obtained by using ultra-high speed photography and the virtual fields method (Method 3). Finally, the time that corresponds to peak stress obtained from reconstructed stress–strain curves (Fig. 7) can also be used to obtain the strain rate that is calculated from real strain gauge history data (Method 4), here shown for the sake of comparison. The data obtained with all methods are presented in Table 4.

The first two methods provide generally lower values of strain rate at the failure location. This is due to the fact

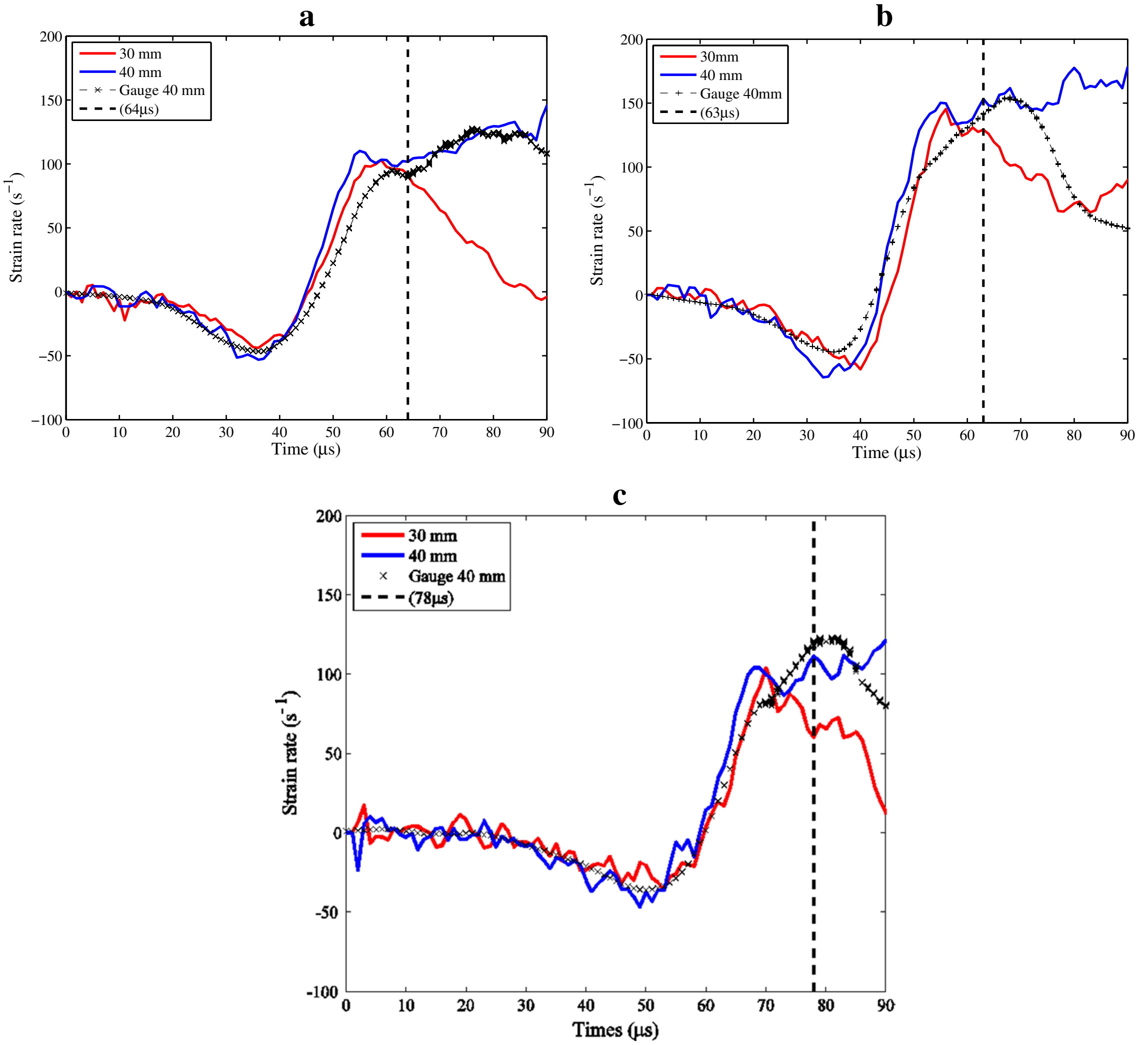

Fig. 9 Strain rate history for three tested samples with virtual gauge at 30 and 40 mm and a real gauge at 40 mm. **a**–sample R30A7-3; **b**-sample R30A7-1; **c**–sample R30A7-2

Table 4 Several methods to obtain the strain rate

Sample	Position	Method 1: (σ_{laser};ε_{gauge})		Method 2: (σ_{VFM};ε_{gauge})		Method 3: (σ_{VFM};ε_{VFM})		Method 4: (t_{VFM};ε_{gauge})	
		Tensile stress	Strain rate	Tensile stress	Strain rate	Tensile stress	Strain rate	Time at peak stress	Strain rate
R30A7-3	40 mm	/	/	6.96	71	6.96	111	78	119
R30A7-1	40 mm	10.6	78	8.81	94	8.81	101	64	92
R30A7-2	40 mm	15.1	117	12.14	120	12.14	153	63	142

that the non-symmetric response of the material is not being taken into account and only the compressive stiffness is used. The methods three and four, which rely on data extracted from VFM processing, provide higher values of local strain rate, which are considered more realistic as there have been no assumptions made on the material behaviour beforehand.

Procedure to Identify Global Young's Modulus

The procedure to identify the average Young's modulus of quasi-brittle materials subjected to dynamic spalling test is based on the analysis already presented in [39] and is obtained by dividing the average virtual work associated to internal and external forces, (Eq. 2), as reported in [77].

The stiffness parameter obtained in this way can also be referred to as the global Young's Modulus as it is derived from temporal acceleration and strain maps averaged on the entire framed sample surface. Figure 10 shows the temporal identification of the global Young's modulus for three spalling tests performed with the corresponding mean values obtained in the compression interval. A more interesting part of the presented results is the second interval which corresponds to tensile loading stage. In both cases, the global Young's modulus values are much lower than in compressive stage and after reaching a local peak decrease towards zero by the end of the acquisition. This was attributed to the damage processes that are triggered during the tensile stage, that finally lead to formation of one or several macro-cracks as discussed in [39].

On the other hand, the values observed in tension differ from the values obtained by performing linear regression of the local virtual gauge response. The sensitivity study performed with the methodology of simulating the entire chain of experimental measurement, based on reproducing the image forming process with finite element computations, showed that the measurement of global Young's Modulus can be quite influenced by various external factors such insufficient lightning, under-sampling of the grid pitch as well as camera noise [78]. Consequently, although the identified response provides reasonable results during the compressive stage, it does not allow for a precise identification of the value of the dynamic modulus in tension due to being sensitive to noise, but rather serves as an indicator that the damage is present in the material. Another reason that prevents the extraction of reliable stiffness values is that the stability of the identification depends on the order of the polynomial used to expand the virtual fields that can over-smooth the values of already low dynamic tensile modulus. Finally, the method only allows the identification of a global stiffness value while on the other hand concrete is a highly heterogeneous material which local stiffness varies with respect to its mesostructure. Nevertheless, the method provides reasonable identification results during the compressive loading stage that are closely consistent with the

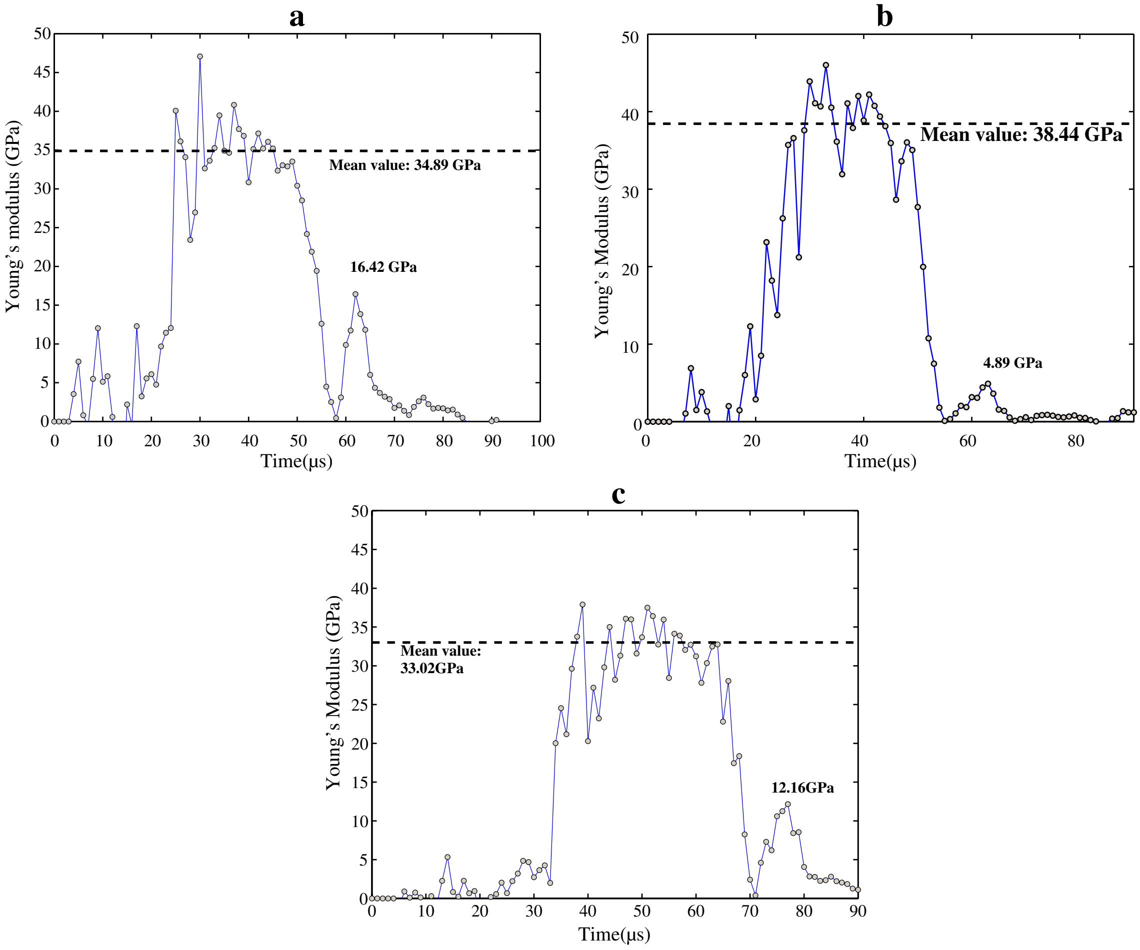

Fig. 10 Identified Young's Modulus for three concrete samples using virtual fields of 8th order polynomial. **a**–sample R30A7-3; **b**-sample R30A7-1; **c**–sample R30A7-2

values of Young's modulus obtained from the measurement of unidimensional wave speed using the time shift between strain gauge and laser interferometer ($E_{dyn} = \rho(C_0)^2$). The results from both methods are summarized in Table 5 where the averaged dynamic Young's modulus in compression is obtained as an overall average on corresponding confidence intervals.

Validation with Numerical Simulation

The previous part of the paper dealt with processing the spalling experiments by using both traditional and full field measurement techniques. The virtual fields method was used to identify the material response from full field displacements using the acceleration maps as an alternative load cell. Then, it was possible to reconstruct the stress–strain curves of each tested sample at any given cross-section visualised with the ultra-high speed camera. The results shown that the value of peak stress obtained from the stress–strain curves was constantly lower than the one obtained with Novikov processing. Furthermore, the identified Young's modulus in dynamic tension was in all cases lower than the stiffness obtained in the compressive stage of the test.

In this section, the effect of the change of Young's modulus on the Novikov processing of test results is explored through explicit FE numerical simulations. A damage model known as the *PRM* model (*Pontiroli, Rouquand and Mazars*) [79, 80] is used to simulate the dynamic spalling tests through a user subroutine. This model permits to explicitly impose the level of tensile strength (peak stress in tension). The model incorporates Mazars damage law [40] and a dissymmetric parameter that can reproduce different linear response of concrete in compression and tension prior the peak stress. The simulation results show that without changing the failure stress criterion, the rear face velocity is largely affected by the dissymmetric concrete response which can ultimately lead to errors in estimating the apparent tensile strength by using the Novikov data processing.

Table 5 Identified dynamic Young's modulus in GPa during the compressive stage of the spalling test by applying virtual fields method and wave speed measurement

Sample	Virtual fields method	Wave speed measurement
R30A7-3	Mean: 33.02 Std: 3.64	42.88
R30A7-2	Mean: 38.44 Std: 4.09	42.61
R30A7-1	Mean: 34.89 Std: 3.62	32.94

Finally, an inverse identification was performed in order to fit the numerically rear face velocity profile to the experimental one up-to the first rebound. It was shown that both peak stress and the stiffness dissymmetry response identified by using the VFM and ultra-high speed displacement measurements need to be taken into account in order to have a good agreement between the numerical and experimental velocity curve. Finally, the validity of traditional processing with using the Novikov formula was discussed, suggesting that one dimensional linear elastic approximation is not a valid tool for retrieving reliable values of spall strength in concrete-like materials.

The PRM Damage Model

The PRM damage model has been developed to simulate the response of concrete material under severe loading conditions, describing the material's response under cyclic and dynamic loading. This model has been extensively used to describe complex phenomena that occur during soft and hard projectile impacts [81, 82]. By relaying on two scalar damage variables that define the damage evolution law separately in compression and tension, the model permits to describe various phenomena related to loss of stiffness under both tensile and compressive loading. Under uniaxial loading condition, where the damage is only considered to take place during the tensile loading, the governing equation of the damage model used is the following:

$$\sigma = E_c\langle\varepsilon\rangle_- + \left(1 - D_t\right)E_t\langle\varepsilon\rangle_+ \tag{4}$$

where σ is the total macroscopic axial stress in the material, $\langle\varepsilon\rangle_-$ and $\langle\varepsilon\rangle_+$ are the negative part and the positive part of the axial strain in compression and tension respectively, E_c and E_t represent linear elastic material stiffness in compression and tension respectively and D_t is the internal damage variable in tension that is in the domain [0−1], where the value 0 corresponds to perfectly elastic virgin material and 1 to completely damaged state. The damage evolution law is dictated by the amount of ultimate deformation that the material can experience during the loading. In the present case, a simplified version of the model was used to describe the material response subjected to tension while in the compression the material is assumed to behave perfectly linearly elastic. The damage starts if the equivalent strain in the material surpasses a threshold value defined as ε_0. The damage evolution law for a uniaxial tensile case reads:

$$\begin{cases} \varepsilon \leqslant \varepsilon_0 \;\rightarrow\; D_t = 0 \\ \varepsilon > \varepsilon_0 \;\rightarrow\; D_t = 1 - \dfrac{\varepsilon_0(1-A)}{\varepsilon} - A\;\omega\;\exp(-B(\omega\varepsilon - \varepsilon_0)) \end{cases} \tag{5}$$

where the constant A is the characteristic material parameter, $B = 1/\varepsilon_0$ is obtained from the ultimate stress criterion $\varepsilon_0 = \sigma_u/E_t$ where the σ_u is the maximal stress limit after which the damage starts taking place and ω is a regularization parameter based on the Hillerborg dissipated energy concept to limit the mesh dependency during strain and damage localization phenomena [83]. The regularization method is introduced by modifying the damage evolution law in such way that it ensures a constant dissipated energy per surface unit in a single finite element regardless of the element size (L_{fe}). To this end, a concept of internal characteristic length is introduced (L_c) based on the defined input fracture energy (G_f). Finally, the regularisation parameter ω is expressed as follows:

$$\omega = \frac{\varepsilon_0}{\varepsilon} + \left(1 - \frac{\varepsilon_0}{\varepsilon}\right)\frac{L_{fe}}{L_c} \quad \text{where } L_c = \mathrm{E}\frac{G_f}{\sigma_u^2} \tag{6}$$

However, the regularization procedure, when used with small finite elements, can lead to a dissipated energy and velocity profile on the rear face that are sensitive to the mesh size [41]. Indeed, it was shown that for a ratio between the internal characteristic length and the finite element size above 4 the dissipated energy substantially increases. In that case, the simulated free-end velocity profiles are strongly affected after the first rebound due to the development of an quasi–elastoplastic stress–strain behaviour caused by reduced mesh size [41]. An adequate mesh size needs to be chosen as compromise between the good spatial discretisation of the numerical model on one hand, and the dissipated energy within the system on the other hand. According to the mesh sensitivity study presented in [41] as a general guideline can be adopted $\frac{\mathrm{L_c}}{\mathrm{L_{fe}}} \leqslant 4$. In the case when the regularization is not used ($\omega = 1$) the description of the damage law becomes simplified as follows:

$$\begin{cases} \varepsilon \leqslant \varepsilon_0 \;\rightarrow\; D_t = 0 \\ \varepsilon > \varepsilon_0 \;\rightarrow\; D_t = 1 - \exp\left(1 - \dfrac{\varepsilon}{\varepsilon_0}\right) \end{cases} \tag{7}$$

The stress evolution of the material response under tension and the corresponding damage evolution law for the case when the regularization is omitted are presented in Fig. 11.

It is worth mentioning that the applied constitutive law perfectly corresponds to the assumptions made when the spall strength is determined using the Novikov processing. The material behaves linearly elastic up-to the ultimate stress is reached after which the response is governed by the damage evolution law.

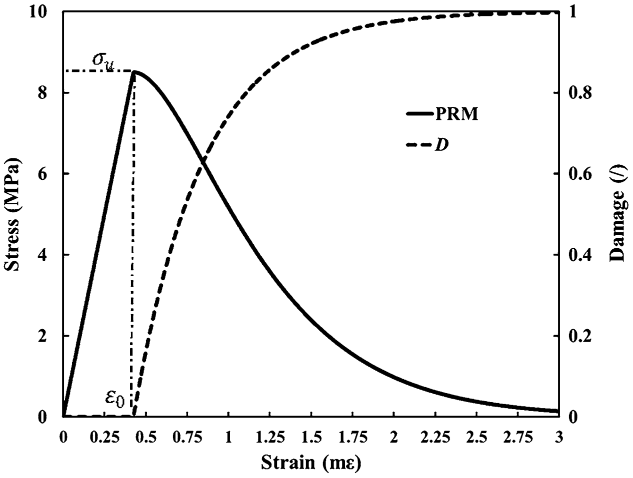

Fig. 11 The tensile behaviour of the PRM model used to simulate the spalling experiments with parameters: $E_c = 35.5$ GPa, $\sigma_u = 8.5$ MPa, $\omega = 1$ and A = 1

Finite Element Simulation and Numerical Results

The 3D finite element model of a spalling sample was created in order to simulate the mechanical response of concrete under dynamic tension using Abaqus/Explicit software. The PRM damage model was implemented in the simulations through a user subroutine VUMAT to describe the material behaviour. The sample geometry is the same as in the experimental part with a length set to 140 mm and a diameter equal to 45.5 mm. The C3D8R elements (three dimensional elements with reduced integration and eight nodes) were used to generate a mesh of 35, 140 elements with the average element size of 2 mm $\left(\frac{\mathrm{L_c}}{\mathrm{L_{fe}}} \leqslant 4\right)$. The mesh size was chosen according to the mesh sensitivity study reported in [41]. The loading boundary condition was considered as a distributed pressure pulse with the temporal distribution obtained from an actual experiment. Instead of simulating the entire spalling setup the experimental loading pulse was applied directly on the bar-specimen interface which was shown to be a good approximation from the numerical point [84]. Numerical simulation showed that the variation of rear face velocity for all nodes is about 1.4% of the average peak nodal velocity. Therefore, the rear face velocity profile was obtained as an average velocity of the entire set of nodes that constitutes the back end of the numerical sample. Furthermore, since the accent is on well simulating the effect of material non-symmetric response on the rear face velocity profile up-to the first rebound, the Hillerborg's regularization technique was be omitted by setting the value ω to 1.

Figure 12 shows the effect of different parameters of the damage model on the rear face velocity profile in the simulated spalling tests. While the ultimate tensile stress only

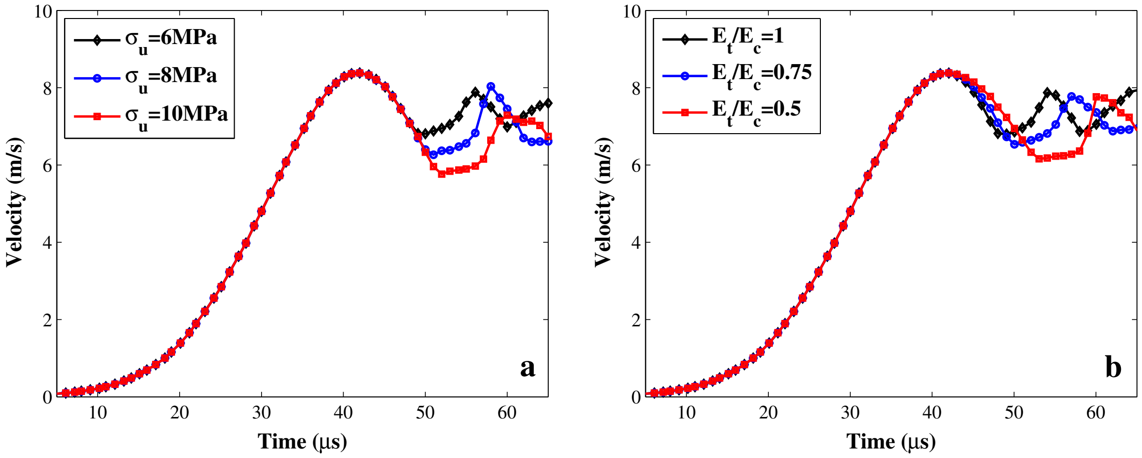

Fig. 12 Results of the numerically simulated rear face velocity profiles: **a** effect of different ultimate strength $E_c = 35.5$ GPa, $E_t/E_c = 1$, $A = 1$, $\rho = 2290\ \mathrm{kg/m^3}$, $\omega = 1$; **b** effect of different dissymmetry factors along with a constant ultimate strength: $E_c = 35.5$ GPa, $\sigma_u = 7$ MPa, $A = 1$, $\rho = 2290\ \mathrm{kg/m^3}$, $\omega = 1$; compressive pulse R30A7-1

influences the value of the velocity rebound as expected (Fig. 12a) a very interesting observation is that the dissymmetrical response, taking into account the different Young's moduli in compression and tension, also has an important effect on the values of the velocity rebound as seen in Fig. 12b. It is clearly observed that the lower the ratio between the tensile and the compressive stiffness the larger is the value of the velocity pullback (the difference between maximal velocity and the velocity at rebound). This further implies that without taking into account the non-symmetric response of concrete in the spalling experiments, the determined values of the apparent spall strength can be overestimated. Finally, it can be also observed that the deceleration part of the velocity profile (after the peak velocity is reached), which corresponds to the compression to tension loading transition, is also affected by the dissymmetry factor. This explains the measured results obtained from the shifted compressive gauge and the laser interferometer in Fig. 3 where indeed in the deceleration part, a misalignment of the two reconstructed stress response curves is also observed.

It has to be mentioned that the PRM model used in these simulations completely adopts the assumptions made on the material behaviour when experimental results are being processed using the acoustic approximation (linear-elasticity up-to peak). Interestingly, the results presented in Fig. 12a indicates that if this assumption as well as the assumption of instantaneous failure were valid, the change in ultimate tensile strength would indeed only influence the velocity rebound. However, the experimental results presented in the first part of this article demonstrated a non-linear response before the peak and a non-symmetric response in compressive and tensile stage, which questions the applicability of the Novikov processing when concrete-like materials are investigated.

Numerical Identification Procedure and Comparison to the Experimental Results

In order to further explore the validity of the identified material response as well as the reliability of the Novikov processing, an inverse identification is performed based on reproducing the rear face velocity profile with the simulated spalling experiments using the PRM damage model. The model assumes a perfect linear-elastic response in compression while describing a damage response in tension along with a reduction of material stiffness prior the stress peak. The FE computations have been performed using the input data obtained from the experimental measurements (compressive pulse) and the numerical results have been compared to the experimentally measured rear-face velocity profile. The comparison between the numerically simulated and experimentally measured rear face velocity profiles for one concrete sample is depicted in Fig. 13. The Hillerborg regularisation technique was used for the sake of obtaining the curves with the similar post rebound response, however, it needs to be mentioned that in this case the most important result to be compared to experimental data concerns the simulated velocity rebound.

The obtained numerical results demonstrate that both the change of the material stiffness and the ultimate tensile strength influence the rear-face velocity pullback. In the present case, the non-symmetric response in compression and tension is considered in the numerical simulations through a bi-linear change in material elastic stiffness while strain softening and loss of tensile stiffness is modelled using Mazars'

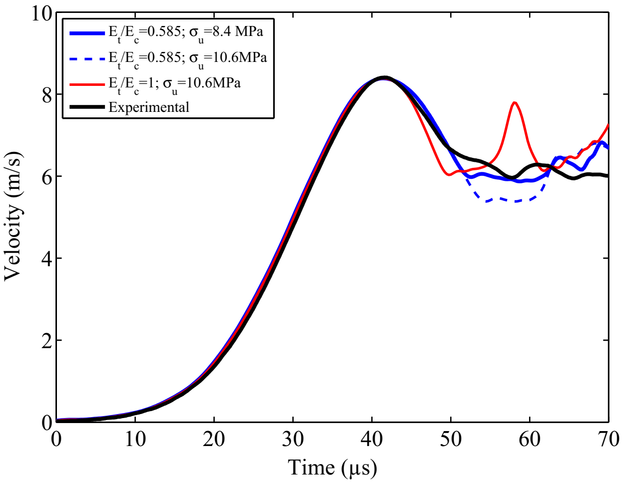

Fig. 13 Results of the inverse identification of the experimental velocity profile using the PRM model and data obtained from the VFM identification (R30A7-1)

damage law. The experimental specimen analysed in the presented case is labelled as R30A7-1 concrete sample. The numerical simulations have been performed for three distinct cases (Fig. 13). First one considers only the input parameters obtained utilizing the traditional processing of experimental data, namely the Novikov ultimate tensile stress (σ_u = 10.6 MPa) and linear symmetric response in compression and tension ($E_t/E_c = 1$). The second case, considers only the data obtained from the virtual fields method processing and full field measurements, namely a lower ultimate tensile stress (σ_u =8.5 MPa) and non-symmetric response in compression and tension ($E_t/E_c = 0.585$). Finally, the third case considers the Novikov ultimate stress (σ_u =10.6 MPa) as the damage onset parameter and the non-symmetric response obtained from applying the virtual fields method ($E_t/E_c = 0.585$), making it a combination of the two processing techniques. The parameters of the PRM model used in the above mentioned numerical simulations are given in Table 6.

The numerical results indicating that the tested sample stayed in the domain of linear elasticity in the compressive stage owing to the fact that that all three simulated velocity profiles well correspond to the experimental curve up-to the peak velocity. The more significant part of the curves is after the peak velocity where the wave reflection takes place. In this domain the numerical curves start to display different tendencies. Both numerical velocity profiles for the first and second case exhibit the same value of the pull-back velocity which is close to the experimental one, even though different ultimate tensile strengths were considered as the input parameters. What seems to be more striking is that if the curve for the second case is treated with the Novikov approach, the failure stress obtained would be close to 10.6 MPa while the ultimate failure stress used as an input in the damage model is 8.5 MPa. Furthermore, it can be observed that the deceleration part of the velocity curve obtained with the VFM data (second case) better matches the experimental one after the peak velocity. The small discrepancies between these two curves can be attributed to the fact that the numerical model used assumes perfect linear elasticity to the peak stress and approximates the non-symmetric response as a bi-linear response. Indeed, in the reconstructed stress–strain curves presented in Fig. 7 it can be seen that the non-symmetric response gradually starts picking up by the end of the compressive phase and then extends to the tensile phase. Both these approximations can be considered to affect the currently simulated velocity profiles. Finally, when the third case is considered, the simulated velocity rebound largely overestimates the experimental response leading to an error of about 15% in pull-back velocity.

The presented results demonstrate that using the assumption of the same dynamic Young's modulus in compression and tension as well as applying the Novikov processing can lead to erroneous values regarding the dynamic tensile strength of brittle materials. Owing to its complex microstructure, concrete material behaves in a non-linear way before the failure takes place. On the other hand, the virtual fields method does not employ any constitutive assumptions on the material behaviour and completely relies on the information embedded in the images capture by an ultra-high imaging system. As such, this method highly depends on the performance of these systems and requires noise reduction methods for extracting meaningful results owing to limited performance of the acquisition systems. However, the future technological

Table 6 Parameters used in the spalling simulations with the PRM model

Case	Data	Density (kg/m^3)	Young's modulus (GPa)	Poisson coefficient	Tensile strength (MPa)	Fracture energy (J/m^2)	L_c (mm)	A	B	Factor of dissymmetry
1	VFM	2290	35.5	0.2	8.5	15	7.37	1	1	0.585
2	Novikov	2290	35.5	0.2	10.6	15	4.74	1	1	1
3	Novikov and VFM	2290	35.5	0.2	10.6	15	4.74	1	1	0.585

advancements in the field of ultra-high speed photography will most certainly bring benefit to these types of inertial experiments.

Conclusion

The spalling technique has been widely adopted as a reliable way of obtaining the dynamic tensile strength of concrete-like materials at intermediate and high strain rates. However, the assumptions made during the traditional Novikov processing of the experiments using the rear-face velocity pull-back remain quite basic when brittle materials such as concretes are investigated. In particular, the assumption that the material behaves linear-elastic up-to the peak tensile stress, when an instantaneous failure occurs which initiates the velocity rebound, and the compressive and tensile elastic moduli are identical are questionable. An attractive alternative is the application of ultra-high speed photography for obtaining full-field measurements and the use of the virtual fields method to identify the material response during the spalling experiments. In this work an ultra-high speed imaging system has been used to film the surface of concrete sample instrumented with a grid pattern in order to measure the temporally resolved displacement fields with 1 μs inter-frame time. Then, the virtual fields method was used to exploit the inertial component of the test, by reconstructing the average stress history in a cross section and the evolution of the average Young's modulus in time. The present part I of the paper presents results of three spalling tests conducted on ordinary concrete samples both using the traditional and VFM processing techniques. The results were compared and the main conclusions are as follows:

- A non-symmetric response in compression and tension is observed in all stress–strain curves reconstructed by using the virtual fields method. The observed tensile stiffness is up-to 50% lower than the initial compressive stiffness. This is then verified with the identification of the temporal evolution of the average Young's modulus. While the average stiffness value in the compressive stage is close to the one obtained with the wave speed measurement, the tensile stiffness modulus is markedly lower and is found to decrease after reaching a critical point owing to damage in the material.
- In all tested samples the peak stress value obtained with the VFM processing was substantially lower than the one obtained with the Novikov approach and the measurement of the velocity pullback.

In order to further investigate the reliability of Novikov processing techniques, numerical simulations have been performed using a damage model that assumes a linear elastic behaviour up-to peak tensile stress and a softening behaviour in the post peak regime. Furthermore, the implemented model allows taking into account the non-symmetric material stiffness in compression and in tension (prior the peak stress). The simulation results are compared to the experimental data with respect to the rear face velocity profiles and the following observations are made:

- While the change of ultimate tensile stress in the damage model only leads to the change of the velocity rebound, the change in the dissymmetry factor of material elastic response influences both the value of the velocity rebound and the deceleration part of the velocity profile. It shows that, for the case of the bilateral material response, the rebound velocity does not represent a reliable way of determining the ultimate tensile strength.
- Only in the case when the experimentally identified values of peak tensile stress and the material non-symmetric stiffness response obtained with the VFM processing are used as input parameters, the numerical simulation was able to well reproduce the rear-face velocity profile. On the other hand, when utilizing the same value of the Young's modulus identified during the compression stage in tensile stage and as well as in the case of using the tensile strength obtained with the Novikov processing as input parameters, numerical computations were not able to faithfully reproduce the rear-face velocity profile from the experiment.

The presented results clearly indicate the sensitivity of the traditional processing of the spalling experiments which is based on the analysis of the rear face profile and the Novikov formula. This processing can lead to erroneous conclusions regarding the tensile strength of brittle materials. The reason is mainly due to the fact that the entire damage history, including pre-peak non-symmetric response caused by micro-cracking is embedded in the measured velocity profile. And if this is not taken into account, the simple acoustic approximation and the velocity pull-back seems not to be valid as a spall criterion. On the other hand, the virtual fields method does not rely on any material constitutive assumptions and instead of one measurement provides rich fields of information that can be used for material identification. This technique allows direct identification of the non-symmetric material response and direct measurement of local strains and strain rates on the sample surface. Furthermore it allows reconstruction of average longitudinal stress profiles using only the acceleration data.

Nevertheless, this technique, although clearly superior to traditional processing, strongly depends on the performance on the ultra-high speed acquisitions systems as well as noise sources that can propagate from the captured images to the identified results. Due to the temporal and spatial noise present in the currently employed imaging system significant low-pass filtering was used in order to extract meaningful identification results. For this reason, recent and future technological advancements in this field regarding the increased stability of the images, as well as spatial and temporal resolution would certainly bring only benefit to this type of diagnostics techniques.

Acknowledgements This research has been performed with the financial support of the CEA-Gramat Research Center (France). The provided support is gratefully acknowledged by the authors. The authors would like also to thank Laurent Sallier for assisting with the experimental work and Dr. Benjamin Erzar (CEA-Gramat) for fruitful discussions. This work has been partially financed by the LabEx Tec 21 (Investissements d'Avenir - Grant Agreement No. ANR-11-LABX-0030). The provided support is gratefully acknowledged by the authors.

References

1. Li QM, Reid SR, Wen HM, Telford AR (2005) Local impact effects of hard missiles on concrete targets. Int J Impact Eng 32:224–284. doi:10.1016/j.ijimpeng.2005.04.005
2. Wen HM, Xian YX (2015) A unified approach for concrete impact. Int J Impact Eng 77:84–96. doi:10.1016/j.ijimpeng.2014.11.015
3. Kanel GI (2010) Spall fracture: methodological aspects, mechanisms and governing factors. Int J Fract 163:173–191. doi:10.1007/s10704-009-9438-0
4. Malvar LJ, Crawford JE (1998) Dynamic Increase Factors. In: 28th Department of defense explosives safety seminar. Orlando, Florida, pp 1–17
5. Weerheijm J. 2013 Understanding the tensile properties of concrete. Woodhead Publishing Limited, Cambridge
6. Zielinski AJ, Reinhard HW, Körmeling HA (1981) Experiments on concrete under uniaxial impact tensile loading. Matériaux Constr 14:163–169. doi:10.1007/BF02473920
7. Zielinski AJ, Reinhardt HW (1982) Stress-strain behaviour of concrete and mortar at high rates of tensile loading. Cem Concr Res 12:309–319
8. Rossi P, Mier JGM., Toutlemonde F, Maou F, Boulay C (1994) Effect of loading rate on the strength of concrete subjected to uniaxial tension. Mater Struct 27:260–264. doi:10.1007/BF02473042
9. Toutlemonde F, Boulay C, Rossi P (1995) High strain rate tensile behaviour of concrete: significan parameters. In Fracture mechanics of concrete structures, Proceedings of FRAMCOS-2. Wittmann FH (ed) pp. 709–718. AEDIFICATIO, Freiburg
10. Weerheijm J. 1992 Concrete under impact tensile loading and lateral compression. PhD thesis, TU Delft
11. Reinhardt HW, Körmeling HA, Zielinski AJ (1986) The split Hopkinson bar, a versatile tool for the impact testing of concrete. Mater Struct 19:55–63. doi:10.1007/BF02472311
12. Asprone D, Cadoni E, Prota A, Manfredi G (2009) Dynamic behavior of a mediterranean natural stone under tensile loading. Int J Rock Mech Min Sci 46:514–520. doi:10.1016/j.ijrmms.2008.09.010
13. Cadoni E, Solomos G, Albertini C (2013) Concrete behaviour in direct tension tests at high strain rates. Mag Concr Res 65:660–672. doi:10.1680/macr.12.00175
14. Cadoni E, Labibes K, Albertini C, Berra M, Giangrasso M (2001) Strain-rate effect on the tensile behaviour of concrete at different relative humidity levels. Mater Struct 34:21–26
15. Lambert DE, Ross CA 2000 Strain rate effects on dynamic fracture and strength. Int J Impact Eng 24, 985–998. doi:10.1016/S0734-743X(00)00027-0
16. Wang QZ, Li W, Xie HP (2009) Dynamic split tensile test of flattened Brazilian disc of rock with SHPB setup. Mech Mater 41:252–260. doi:10.1016/j.mechmat.2008.10.004
17. Chen R, Xia K, Dai F, Lu F, Luo SN (2009) Determination of dynamic fracture parameters using a semi-circular bend technique in split Hopkinson pressure bar testing. Eng Fract Mech 76:1268–1276. doi:10.1016/j.engfracmech.2009.02.001
18. Dai F, Xia K, Zheng H, Wang YX (2011) Determination of dynamic rock Mode-I fracture parameters using cracked chevron notched semi-circular bend specimen. Eng Fract Mech 78:2633–2644. doi:10.1016/j.engfracmech.2011.06.022
19. Delvare F, Hanus JL, Bailly P (2010) A non-equilibrium approach to processing Hopkinson Bar bending test data: Application to quasi-brittle materials. Int J Impact Eng 37:1170–1179. doi:10.1016/j.ijimpeng.2010.07.001
20. Zhao J, Li H (2000) Experimental determination of dynamic tensile properties of a granite. Int J Rock Mech Min Sci 37:861–866. doi:10.1016/S1365-1609(00)00015-0
21. Bragov AM, Petrov YV, Karihaloo BL, Konstantinov AY, Lamzin DA, Lomunov AK, Smirnov, IV (2013) Dynamic strengths and toughness of an ultra high performance fibre reinforced concrete. Eng Fract Mech 110:477–488. doi:10.1016/j.engfracmech.2012.12.019
22. Lu YB, Li QM (2011) About the dynamic uniaxial tensile strength of concrete-like materials. Int J Impact Eng 38:171–180. doi:10.1016/j.ijimpeng.2010.10.028
23. Forquin P, Riedel W, Weerheijm J (2013) Dynamic test devices for analyzing the tensile properties of concrete. In Understanding the tensile properties of concrete, pp 137e–181e. Elsevier, Amsterdam. doi:10.1533/9780857097538.2.137
24. Klepaczko JRR, Brara A (2001) An experimental method for dynamic tensile testing of concrete by spalling. Int J Impact Eng 25:387–409. doi:10.1016/S0734-743X(00)00050-6
25. Schuler H, Mayrhofer C, Thoma K (2006) Spall experiments for the measurement of the tensile strength and fracture energy of concrete at high strain rates. Int J Impact Eng 32:1635–1650. doi:10.1016/j.ijimpeng.2005.01.010
26. Weerheijm J, Van Doormaal, JC (2007) Tensile failure of concrete at high loading rates: new test data on strength and fracture energy from instrumented spalling tests. Int J Impact Eng 34:609–626. doi:10.1016/j.ijimpeng.2006.01.005
27. Kubota S, Ogata Y, Wada Y, Simangunsong G, Shimada H, Matsui K (2008) Estimation of dynamic tensile strength of sandstone. Int J Rock Mech Min Sci 45:397–406. doi:10.1016/j.ijrmms.2007.07.003
28. Zhu J, Sun C, Qian Z, Chen J (2011) The spalling strength of ultra-fiber reinforced cement mortar. Eng Fail Anal 18:1808–1817. doi:10.1016/j.engfailanal.2011.05.001
29. Zhang QB, Zhao J (2014) A review of dynamic experimental techniques and mechanical behaviour of rock materials. Rock Mech Rock Eng 47:1411–1478. doi:10.1007/s00603-013-0463-y
30. Erzar B, Forquin P (2010) An experimental method to determine the tensile strength of concrete at high rates of strain. Exp Mech 50:941–955. doi:10.1007/s11340-009-9284-z
31. Novikov SA, Ivanov AG (1966) Failure of steel, aluminium and copper under explosive shock loading. Fiz Met i Metalloved 21:608–615
32. Erzar B, Forquin P (2014) Analysis and modelling of the cohesion strength of concrete at high strain-rates. Int J Solids Struct 51:2559–2574. doi:10.1016/j.ijsolstr.2014.01.023
33. Li X, Tao M, Wu C, Du K, Wu Q (2017) Spalling strength of rock under different static pre-confining pressures. Int J Impact Eng 99:69–74. doi:10.1016/j.ijimpeng.2016.10.001

34. Snozzi L, Gatuingt F, Molinari JF (2012) A meso-mechanical model for concrete under dynamic tensile and compressive loading. Int J Fract 178:179–194. doi:10.1007/s10704-012-9778-z
35. Xu PB, Xu H, Wen HM 2016 3D meso-mechanical modeling of concrete spall tests. Int J Impact Eng. 97, 46–56. doi:10.1016/j.ijimpeng.2016.06.005
36. Zhou W, Tang L, Liu X, Ma G, Chen M (2016) Mesoscopic simulation of the dynamic tensile behaviour of concrete based on a rate-dependent cohesive model. Int J Impact Eng 95:165–175. doi:10.1016/j.ijimpeng.2016.05.003
37. Pedersen RR, Simone A, Sluys LJ (2013) Mesoscopic modeling and simulation of the dynamic tensile behavior of concrete. Cem Concr Res 50:74–87. doi:10.1016/j.cemconres.2013.03.021
38. Erzar B, Forquin P (2011) Experiments and mesoscopic modelling of dynamic testing of concrete. Mech Mater 43:505–527. doi:10.1016/j.mechmat.2011.05.002
39. Pierron F, Forquin P (2012) Ultra-high-speed full-field deformation measurements on concrete spalling specimens and stiffness identification with the virtual fields method. Strain 48:388–405. doi:10.1111/j.1475-1305.2012.00835.x
40. Mazars J (1986) A description of micro- and macroscale damage of concrete structures. Eng Fract Mech 25:729–737. doi:10.1016/0013-7944(86)90036-6
41. Sallier L, Forquin P (2012) On the use of Hillerborg regularization method to model the softening behaviour of concrete subjected to dynamic tensile loading. Eur Phys J Spec Top 206:97–105. doi:10.1140/epjst/e2012-01591-5
42. Hentz S, Donzé FV, Daudeville L (2004) Discrete element modelling of concrete submitted to dynamic loading at high strain rates. Comput Struct 82:2509–2524. doi:10.1016/j.compstruc.2004.05.016
43. Weerheijm J, Van Doormaal A (2004) Tensile fracture of concrete at high loading rates. FRAMCOS – 5, Vail
44. Wu H, Zhang Q, Huang F, Jin Q (2005) Experimental and numerical investigation on the dynamic tensile strength of concrete. Int J Impact Eng 32:605–617. doi:10.1016/j.ijimpeng.2005.05.008
45. Brara a., Klepaczko JR (2006) Experimental characterization of concrete in dynamic tension. Mech Mater 38:253–267. doi:10.1016/j.mechmat.2005.06.004
46. Gabet T, Malécot Y, Daudeville L (2008) Triaxial behaviour of concrete under high stresses: influence of the loading path on compaction and limit states. Cem Concr Res 38:403–412. doi:10.1016/j.cemconres.2007.09.029
47. Piotrowska E, Forquin P (2015) Experimental investigation of the confined behavior of dry and wet high-strength concrete: quasi static versus dynamic loading. J Dyn Behav Mater 1:191–200. doi:10.1007/s40870-015-0017-3
48. Zingg L, Briffaut M, Baroth J, Malecot Y (2016) Influence of cement matrix porosity on the triaxial behaviour of concrete. Cem Concr Res 80:52–59. doi:10.1016/j.cemconres.2015.10.005
49. Poinard C, Piotrowska E, Malecot Y, Daudeville L, Landis EN (2012) Compression triaxial behavior of concrete: the role of the mesostructure by analysis of X-ray tomographic images. Eur J Environ Civ Eng 16:s115–s136. doi:10.1080/19648189.2012.682458
50. Parks VJ (1989) Geometrie Moire. In: Pendleton RL, Tuttle ME (eds) Manual on experimental methods for mechanical testing of composites. Springer, Dordrecht, pp 57–65. doi:10.1007/978-94-009-1129-1_11
51. Piro JL, Grediac M (2004) Producing and transferring low-spatial-frequency grids for measuring displacement fields with Moire and grid methods. Exp Tech 28:23–26
52. Pierron F, Grediac M 2012 The virtual fields method. 1st edn. Springer, New York. doi:10.1007/978-1-4614-1824-5
53. Giraudeau A, Pierron F (2005) Identification of stiffness and damping properties of thin isotropic vibrating plates using the virtual fields method: theory and simulations. J Sound Vib 284:757–781. doi:10.1016/j.jsv.2004.07.009
54. Giraudeau A, Guo B, Pierron F (2006) Stiffness and damping identification from full field measurements on vibrating plates. Exp Mech 46:777–787. doi:10.1007/s11340-006-9477-7
55. Moulart R, Pierron F, Hallett SR, Wisnom MR (2011) Full-field strain measurement and identification of composites moduli at high strain rate with the virtual fields method. Exp Mech 51:509–536. doi:10.1007/s11340-010-9433-4
56. Pierron F, Zhu H, Siviour C (2014) Beyond Hopkinson's bar. Philos Trans A 372:20130195. doi:10.1098/rsta.2013.0195
57. Yoon S-H, Siviour CR (2017) Application of the virtual fields method to rubbers under medium strain rate deformation using both acceleration and traction force data. J Dyn Behav Mater 3:12–22. doi:10.1007/s40870-016-0090-2
58. Yoon S, Giannakopoulos I, Siviour CR (2015) Application of the virtual fields method to the uniaxial behavior of rubbers at medium strain rates. Int J Solids Struct 69–**70**:553–568. doi:10.1016/j.ijsolstr.2015.04.017
59. Wang D, Lucas M, Tanner KE (2013) Characterising the strain and temperature fields in a surrogate bone material subject to power ultrasonic excitation. Strain 49:409–419. doi:10.1111/str.12047
60. Pierron F (2016) Addendum to 'characterising the strain and temperature fields in a surrogate bone material subject to power ultrasonic excitation'. Strain 52:186–190. doi:10.1111/str.12180
61. Surrel Y (1994) Moire and grid Methods: a 'signal processing' approach. Photomechanics 2342:118–127
62. Grédiac M, Blaysat B, Sur F (2017) A critical comparison of some metrological parameters characterizing local digital Image correlation and grid method. Exp Mech. doi:10.1007/s11340-017-0279-x
63. Zhu H, Pierron F (2016) Exploration of Saint-Venant's principle in inertial high strain rate testing of materials. Exp Mech 56:3–23. doi:10.1007/s11340-015-0078-1
64. Zhao B, Asundi A (2001) Microscopic grid methods—resolution and sensitivity. Opt Lasers Eng 36:437–450. doi:10.1016/S0143-8166(01)00071-9
65. Saletti D, Forquin P (2015) A comparison of DIC and grid measurements for processing spalling tests with the VFM and an 80-kpixel ultra-high speed camera. Eur Phys J Spec Top 225:311–323. doi:10.1140/epjst/e2015-77777-x
66. Grédiac M, Sur F, Blaysat B (2016) The Grid method for in-plane displacement and strain measurement: a review and analysis. Strain 52:205–243. doi:10.1111/str.12182
67. Kosonocky WF, Yang G, Ye C, Kabra RK, Xie L, Lawrence JL, Mastrocolla V, Shallcross FV, Patel V (1996) 360/spl times/360-element very-high-frame-rate burst image sensor. Solid-state circuits conference, 1996. Digest of technical papers. 42nd ISSCC., 1996 IEEE international, pp 182–183. doi:10.1109/ISSCC.1996.488562
68. Etoh TG et al. (2003) An image sensor which captures 100 consecutive frames at 1,000,000 frames/s. IEEE Trans Electron Dev 50:144–151. doi:10.1109/TED.2002.806474
69. Etoh TG, Son DVT, Yamada T, Charbon E (2013) Toward one giga frames per second-evolution of in situ. Storage Image Sens 13:4640–4658. doi:10.3390/s130404640
70. Badulescu C, Grediac M, Mathias JD (2009) Investigation of the grid method for accurate in-plane strain measurement. Meas Sci Technol 20:9
71. Rossi M, Pierron F, Forquin P (2014) Assessment of the metrological performance of an in situ storage image sensor ultra-high speed camera for full-field deformation measurements. Meas Sci Technol 25:25401. doi:10.1088/0957-0233/25/2/025401
72. Avril S, Feissel P, Pierron F, Villon, P (2008) Estimation of the strain field from full-field displacement noisy data. Comparing

finite elements global least squares and polynomial diffuse approximation. Eur J Comput Mech 17:857–868. doi:10.3166/remn.17.857-868

73. Avril S, Feissel P, Pierron F, Villon P (2010) Comparison of two approaches for differentiating full-field data in solid mechanics. Meas Sci Technol 21:15703. doi:10.1088/0957-0233/21/1/015703
74. Savitzky A, Golay MJE (1964) Smoothing and differentiation of data by simplified least squares procedures. Anal Chem 36:1627–1639. doi:10.1021/ac60214a047
75. Saadati M, Forquin P, Weddfelt K, Larsson PL (2016) On the tensile strength of granite at high strain rates considering the influence from preexisting cracks. Adv Mater Sci Eng **2016**. doi:10.1155/2016/6279571
76. Forquin P, Erzar B (2009) Dynamic fragmentation process in concrete under impact and spalling tests. Int J Fract 163:193–215. doi:10.1007/s10704-009-9419-3
77. Pierron F, Forquin P (2012) The virtual fields method applied to spalling tests on concrete. EPJ Web Conf 26:1054. doi:10.1051/epjconf/20122601054
78. Lukić B, Saletti D, Forquin P (2017) Use of simulated experiments for material characterization of brittle materials subjected to high strain rate dynamic tension. Philos Trans R Soc A Math Phys Eng Sci 375:20160168. doi:10.1098/rsta.2016.0168
79. Pontiroli C, Rouquand A, Mazars J (2010) Predicting concrete behaviour from quasi-static loading to hypervelocity impact. Eur J Environ Civ Eng 14:703–727. doi:10.1080/19648189.2010.9693259
80. Rouquand A, Pontiroli C, Mazars J 2007 Concrete structures under severe loading: a strategy to model the response for a large range of dynamic loads. In Fracture mechanics of concrete and concrete structures: proceedings of FraMCoS-6, Catania, Italy
81. Pontiroli C, Rouquand A, Daudeville L, Baroth J (2012) Soft projectile impacts analysis on thin reinforced concrete slabs: tests, modelling and simulations. Eur J Environ Civ Eng 16:1058–1073. doi:10.1080/19648189.2012.699745
82. Pontiroli C, Erzar B, Buzaud E (2014) Concrete behaviour under ballistic impacts: effects of materials parameters to penetration resistance and modeling with PRM model. Comput Model Concr Struct Proc EURO-C 2014 v2:685–693
83. Hillerborg A, Modéer M, Petersson P-E (1976) Analysis of crack formation and crack growth in concrete by means of fracture mechanics and finite elements. Cem Concr Res 6:773–781. doi:10.1016/0008-8846(76)90007-7
84. Lu Y, Xu J, Weerheijm J (2013) A mesoscale modeling perspective of cracking process and fracture energy under high strain rate tension. In 8th International Conference on Fracture Mechanics of Concrete and Concrete Structures - FraMCoS-*8*. Van Mier JGM, Ruiz G, Andrade C, Yu RC, Zhang XX (eds), pp. 942–952. Toledo, Spain